JOURNAL OF CATALYSIS 98, 326–334 (1986)

Supported Uranium Oxides as Oxidation Catalysts

I. Synthesis and Characterization of Uranium Oxides on Al_2O_3, SiO_2, TiO_2, and MgO Supports

H. COLLETTE,[1] S. MAROIE,[2] J. RIGA, J. J. VERBIST, Z. GABELICA, J. B.NAGY, AND E. G. DEROUANE

Groupe de Chimie Physique, Facultés Universitaires Notre-Dame de la Paix, 61 Rue de Bruxelles, B-5000 Namur, Belgium

Received July 18, 1985; revised October 10, 1985

Supported uranium oxides were prepared on commercial SiO_2, TiO_2, Al_2O_3, and MgO carriers, and characterized by a variety of physicochemical techniques. Simultaneous thermoanalytical techniques (TG, DTA, DTG) allowed a mechanism to be proposed explaining the formation and stabilization of these catalysts. Combined X-ray Photoelectron Spectroscopy (XPS), Energy Dispersive X-Ray Analysis (EDX), and analytical electron microscopy were used to probe the dispersion of the active phase on each support, as a function of the calcination temperature. Encapsulation phenomena of the active phase (UO_x) by the support were observed in the case of SiO_2- and TiO_2-based catalysts calcined at 900°C. Strong oxide–oxide interaction was postulated to explain the corresponding XPS chemical shift of the uranium level. Segregation of UO_x species probably occurs on the more refractory supports, e.g., Al_2O_3 and MgO.

INTRODUCTION

Transition element-based catalysts are widely used for a variety of catalytic reactions, because of the ability of their delocalized *p* or *d* orbitals to interact with numerous organic and inorganic compounds. By analogy, the actinide elements offer an electronic structure which can be described as a random-like core of 86 e^- surrounded by valence electrons in 7*s*, 6*d*, and 5*f* shells. These 5*f* electrons are more delocalized than the 4*f* electrons of the lanthanides and thus confer on the actinides properties which may resemble those of the elements belonging to Group IB through VIIB and to Group VIII ("*d*-block" elements). Moreover, the particular spatial symmetry of the *f*-orbitals, and hence their ability to achieve high coordination numbers, makes these elements good candidates as potential catalysts.

It is hence not surprising that uranium oxides have been reported as catalysts for many applications. Pure uranium oxides are active for the dehydrogenation and dehydration of ethanol (*1*) and 2-propanol (*2*), and the dehydrogenation of ethylbenzene (*3*). They also show interesting catalytic properties for the oxidation of CO by oxygen (*4, 5*).

Their composition with other oxides is known to improve their catalytic behavior. For example, uranium–antimony mixed oxides are well known as propylene ammoxidation catalysts (*6–11*), and uranium–bismuth oxide catalysts are active for the oxidative demethylation of toluene (*12, 13*). Moreover, the presence of alkali and alkaline-earth elements increase their activity for the oxidation of CO by NO (*14*).

As part of a more general investigation of the relationships existing between the electronic structure and the activity of uranium mixed oxide catalysts, uranium oxides supported by various carriers were synthesized. Their preparation and thorough physicochemical characterization by a vari-

[1] To whom queries on this paper should be addressed.

[2] Present address: Essochem Europe Inc., B-1920 Machelen, Belgium.

0021-9517/86 $3.00

ety of techniques are reported in this paper. Specific information about the dispersion of the supported phases is inferred from combined X-ray photoelectron spectroscopy (XPS), energy dispersive X-ray analysis (EDX), and analytical electron microscopy results. A forthcoming paper will correlate these data with activity measurements for the catalytic oxidation of CO by O_2 (*15*).

EXPERIMENTAL

1. Catalyst Preparation

Supported uranium (10 at.wt.%) oxide catalysts were prepared by impregnating commercial supports, i.e., SiO_2 (silica gel Davison grade 950), TiO_2 (Degussa P25), Al_2O_3 (Degussa type C), and MgO (Merck), with aqueous solutions of uranyl nitrate ($UO_2(NO_3)_2$). The resulting solutions were slowly evaporated and the solids obtained were dried overnight at 110°C. They were then calcined for 16 h in air at 500, 700, or 900°C, respectively. Impregnation was assumed to be quantitative. They are designated as UO_x–*S* samples, *S* indicating the nature of the support. UO_x species will be referred to as the "active phase."

2. Characterization Techniques

X-Ray diffraction (XRD) powder patterns were obtained with a Philips PW 1730 diffractometer, at room temperature and using Ni-filtered Cu$K\alpha$ radiation, in order to identify the crystalline compounds present in each system.

Specific surface areas, pore volumes, and pore size distributions were determined by the conventional BET method with nitrogen as adsorbate (*16*).

Particle sizes were estimated by transmission electron microscopy (TEM) using a Philips EM 301 microscope. Samples were deposited on a Cu grid after ultrasonic dispersion in butanol. Morphologies were also evaluated by scanning electron microscopy (SEM) (JEOL JSM-35 instrument).

Analyses for Si, Al, Mg, Ti, and U contents of the catalysts were performed by energy dispersive X-ray analysis (EDX). The samples were glued to a brass support and examined with a JEOL SEM microscope fitted with an energy dispersion X-ray analyzer (μx analytical spectrometer Kevex Unispec System 7000), equipped with a high-resolution semiconductor detector (Kevex Model 2003 Si(Li) with a Be window), allowing the detection of all elements with $Z > 10$.

Note that EDX, which probes ca. 2–4 μm in depth, is a bulk analytical method which analyzes the entirety of small particles but only the outer region of larger crystallites.

Quantification of the EDX results was achieved by computer integration of the specific X-ray lines of the elements to be analyzed, after elimination of the Bremsstrahlung radiation background.

Surface composition was determined by X-ray photoelectron spectroscopy (XPS). The samples were pelleted and deposited on a gold-plated sample holder. XPS spectra were recorded on a Hewlett–Packard 5950 A spectrometer using monochromatized Al$K\alpha$ radiation ($h\nu$ = 1486.6 eV). An electron "flood-gun" was utilized to compensate surface charging effects. Absolute binding energy values (E_b) were obtained by reference to the Au $4f_{7/2}$ level (E_b = 84.0 eV), originating from a vacuum-deposited gold layer.

Combined thermoanalytical methods (simultaneous thermogravimetry (TG), differ-

TABLE 1

Phases Detected by X-Ray Powder Diffraction

Catalyst	Calcination temperature (°C)	Phases
UO_x–TiO_2	500, 700	TiO_2 (anatase) + TiO_2 (rutile)
	900	TiO_2 (rutile)
UO_x–SiO_2	500, 700	Amorphous
	900	U_3O_8
UO_x–Al_2O_3	500, 700	Amorphous
	900	U_3O_8
UO_x–MgO	500, 700, 900	MgO

TABLE 2

Specific Surface Areas and Pore Volumes Determined by BET Measurements for the Various UO_x–Support Systems

Sample	Calcination temperature (°C)	Specific surface area (m^2/g)	Pore volume (cm^3/g)
UO_x–TiO_2	500	49	0.44
	700	34	0.55
	900	6	0.14
UO_x–Al_2O_3	500	90	0.66
	700	88	0.67
	900	60	0.69
UO_x–SiO_2	500	412	0.35
	700	362	0.33
	900	291	0.27
UO_x–MgO	500	31	0.61
	700	24	0.37
	900	6	0.10

ential thermogravimetry (DTG), and differential thermal analysis (DTA)) were used to investigate the physical and chemical transformations occurring during the calcination of the precursors and to elucidate the mechanisms governing the formation of active phases at high temperatures. About 50 mg of sample were heated (20°C min^{-1}) from 20 to 900°C, under static air, in a Stanton-Redcroft STA-780 thermobalance. α-Al_2O_3 was used as DTA reference.

RESULTS AND DISCUSSION

1. X-Ray Diffraction

A phase transformation for TiO_2 (anatase to rutile) was clearly detected by X-ray diffraction above 700°C. For the catalysts with amorphous supports (SiO_2, Al_2O_3), the X-ray powder patterns also revealed the presence of crystalline U_3O_8 at 900°C (Table 1).

However, a very highly dispersed active phase will not show an XRD pattern due to X-ray line broadening, which may be the case for the low-temperature catalysts. Sintering at high temperature could reverse this situation. Consequently, the absence of a diffraction pattern may be indicative of a well-dispersed catalyst. No new lines were found which could have indicated the formation of new compounds by reaction of the carrier with the active phase.

2. BET Analysis

All supported catalysts show a decrease of their specific surface area and changes in their pore size distribution (UO_x–SiO_2 excepted) during calcination, due to sintering and/or structural modification of the supports and/or the active phase (Table 2). Interestingly, the pore volume remains constant for all calcination temperatures when Al_2O_3 is used as support. Figure 1 shows the variation of the pore size distribution of the supported catalysts as a function of calcination temperature. BET analysis confirms that Al_2O_3 (Degussa type C), TiO_2 (Degussa P25), and MgO (Merck) essentially behave as nonmicroporous materials. In contrast, UO_x–SiO_2 possesses a totally microporous system ($d < 50$ Å), which is consistent with its high specific surface area (>300 m^2/g). At high temperature (900°C), Al_2O_3 and TiO_2 show an important conversion from mesopores ($50 < d < 400$ Å) to macropores ($d > 400$ Å), whereas for MgO micropores ($d < 50$ Å) and mesopores ($50 < d < 400$ Å) predominate. These observations can be correlated with catalytic activity measurements (*15*).

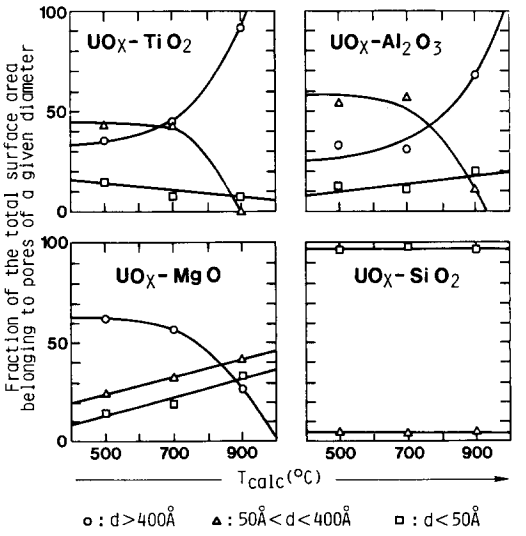

FIG. 1. Influence of calcination temperature on pore size distribution of supported uranium oxide catalysts (BET analysis).

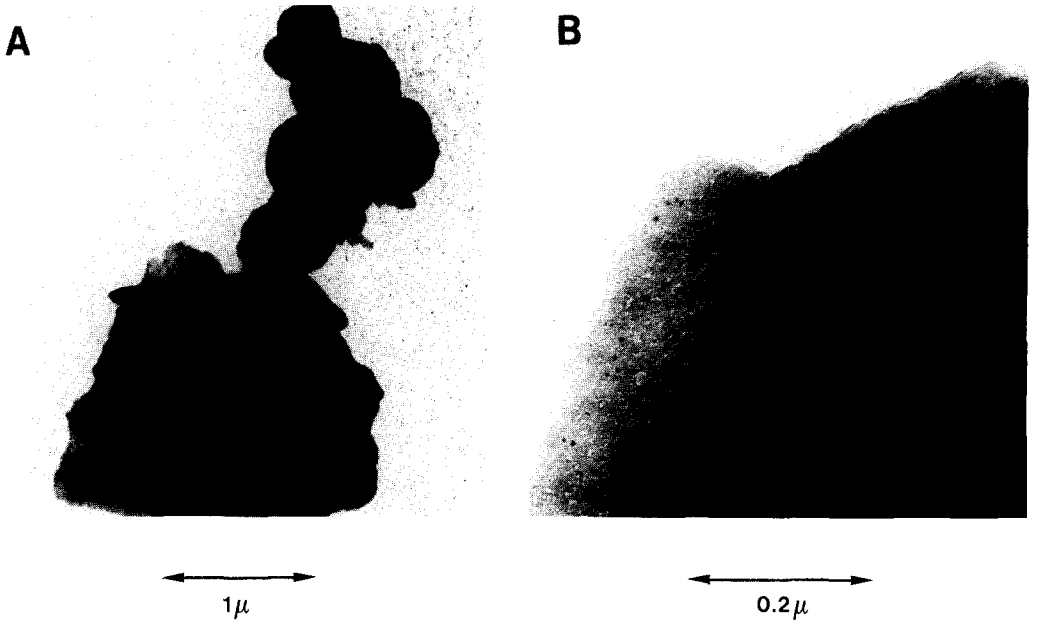

FIG. 2. Transmission electron micrographs of the UO_x–SiO_2 sample calcined at 900°C. Magnifications: 25,000× (A), 150,000× (B).

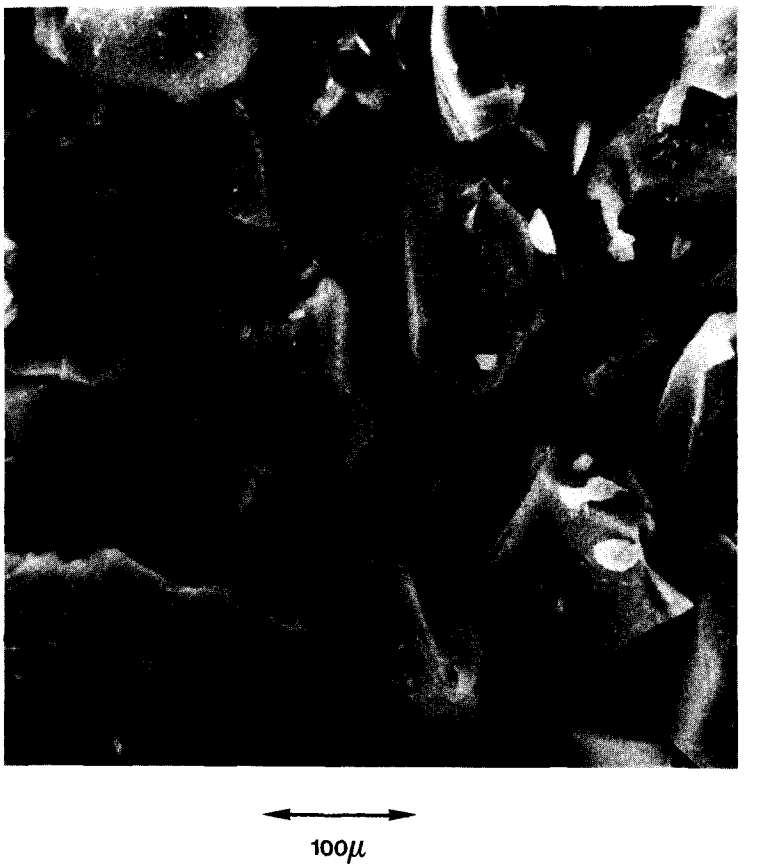

FIG. 3. Scanning electron micrograph of the UO_x–SiO_2 sample calcined at 900°C. Magnification: 200×.

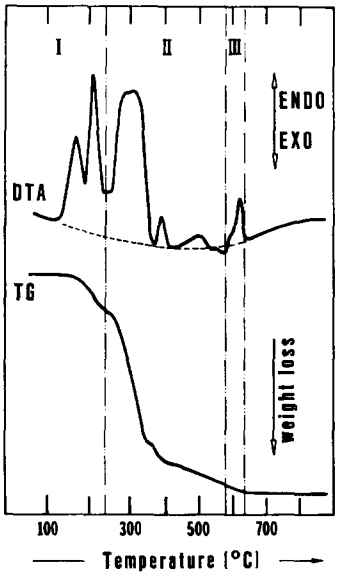

FIG. 4. Thermal decomposition of $UO_2(NO_3)_2 \cdot H_2O$ in static air as studied by combined TG-DTA.

3. *Electron Microscopy*

On SiO_2, following calcination at 900°C, U_3O_8 particles are clearly detected by TEM as dark spots on light support grains (Fig. 2). The average diameter of these particles is estimated to be about 50 Å. The corresponding scanning electron micrograph is shown in Fig. 3. Focused EDX measurements indicate that all the catalysts exhibit nearly homogeneous compositions, i.e., uniform distributions of the active phase.

4. *Thermal Analysis*

Thermal analysis helps elucidation of the mechanisms governing the formation and stabilization of the active phase on the various supports. Figure 4 illustrates the thermal decomposition of pure uranyl nitrate, $UO_2(NO_3)_2$ (precursor to U_3O_8). Three separate temperature ranges can be distinguished. First, dehydration occurs below 225°C. It is characterized by two endothermic peaks at 175 and 210°C, respectively, which correspond to the loss of one molecule of water per $UO_2(NO_3)_2$ unit formula. The second domain (225–580°C) corresponds to the thermolysis of the nitrate ion (endotherms at 290, 310, 395, and 510°C). UO_3 is the product of this decomposition. It is then reduced to $UO_{2.9}$ (peak EXO at 590°C) and ultimately to U_3O_8 (peak ENDO at 630°C) which is stable at 900°C (range III).

Figure 5 compares the thermal analysis data (DTA) for the same compound deposited on the various supports. The supports present a continuous weight loss up to 900°C because of dehydration and progressive dehydroxylation, which partly mask the uranyl nitrate decomposition TG information. However, DTA is able to discriminate between these effects and to point out the role of the different carriers during calcination to obtain the catalysts (Fig. 5). Thermal effects associated with the nitrate decomposition (peaks B) and with support transformations (peaks A, C) can be re-

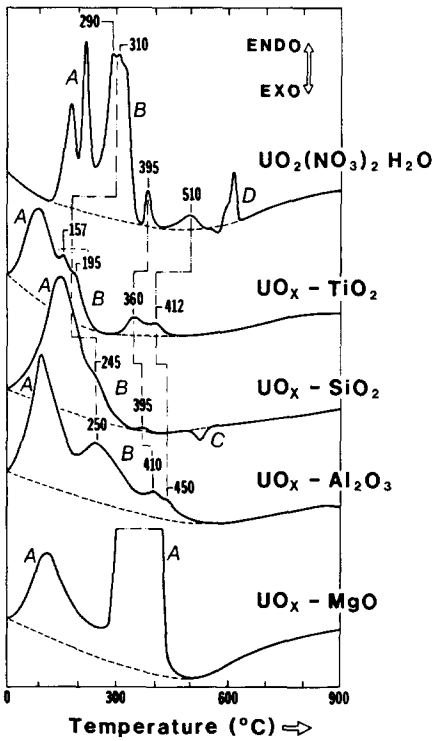

FIG. 5. Comparative DTA traces of various supported uranium oxides during calcination in air at 900°C. (A) Dehydration, (B) uranyl nitrate decomposition, (C) dehydroxylation of SiO_2 (silica gel, Davison), (D) UO_3 reduction.

solved. In the particular case of MgO, which in fact becomes largely $Mg(OH)_2$ following aqueous impregnation, the dehydration phenomenon leading to MgO is so important that all other thermal effects are masked. By comparison with pure uranyl nitrate, all the carriers appear to destabilize the supported uranium compound by favoring its decomposition at lower temperature in the order $TiO_2 > SiO_2 > Al_2O_3$. These interactions with the supports should be reflected in the final dispersion state of the active phase. Finally, TG-DTA proved an adequate technique to identify the presence of residual nitrates that can further influence the catalytic behavior of these systems. A specific thermal effect was observed on SiO_2-supported catalyst (peak C). This irreversible exothermic effect is exclusively present when Davison silica gel exposed to water is heated. The associated weight loss is possibly explained by a high-temperature condensation of silanol groups.

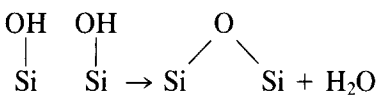

5. X-Ray Photoelectron Spectroscopy

XPS was used essentially in the present case as a surface analytical technique, for two main purposes:

(i) the identification of the surface uranium compounds formed by calcination (evidence for electronic interaction between the carrier and the active phase may also be obtained from XPS chemical shifts);

(ii) the determination of the surface compositions of the catalysts as a function of calcination temperature.

Binding energies (BE) and linewidths (LW) of U $4f$ and $M\,2p$ (M = Si, Al, Ti, Mg) peaks are listed in Table 3. For the Al_2O_3-, TiO_2-, and MgO-supported catalysts, calcination temperature does not influence the nature of the uranium oxide species. U $4f_{7/2}$ binding energy values are close to those reported for U_3O_8 (*17*). However, these results do not exclude the possibility of an interaction between the support and the UO_x phase. Indeed, if interaction takes place only at the interface between UO_x and the support, bulky UO_x crystallites (diameter of about 20 nm) could have a significant number of surface atoms which are not interacting with the carrier.

For the system UO_x–SiO_2 calcined at 900°C, the $4f_{7/2}$ level of uranium is broadened and shifted to lower BE values. This observation reveals a strong interaction between UO_x and SiO_2 which is favored by the high degree of dispersion of the active phase. Such a strong oxide–oxide interaction (SOOI) has been proposed earlier by Lund and Dumesic for the Fe_3O_4–SiO_2 system (*18–21*). The aforementioned XPS binding energy shift may stem from two effects.

(i) The net charge on uranium is modified through electronic interactions with the carrier (more precisely, the observed lower binding energy for U $4f_{7/2}$ would then reflect an electronic transfer from the support to UO_x).

(ii) More effective extraatomic relaxation coming from the molecular orbitals of the support in response to the creation of a core hole during photoionization of uranium atoms.

In addition to the BE shift, the linewidth increase at 900°C (Table 3) could result from a distribution of support interactions or from uranium species in different chemical environments. Based on the XPS quantitative analysis, a model can be proposed to explain the specific interaction observed for the UO_x–SiO_2 system calcined at 900°C (see below). Let us note that massive formation of a mixed oxide between SiO_2 and U_3O_8 can be rejected, as only crystalline U_3O_8 aggregates were detected by XRD.

The variation of the intensity ratios between uranium (I_U) and characteristic carrier (I_c) XPS lines ($I_{U\,4f_{7/2}}/I_{M\,2p}$) is compared with corresponding EDX analyses ($I_{UM\alpha\,(1,2)}/I_{MK\alpha\,(1,2)}$) in Fig. 6. As expected, bulk compositions estimated by EDX do

TABLE 3

XPS Analysis: Binding Energies (E_b) and Linewidths (LW) of U $4f_{7/2}$ and M $2p$ Signals (M = Si, Al, Mg, Ti)

Catalyst	Calcination temperature (°C)	Support		Uranium oxide	
		Reference peak E_b (eV)	LW (eV)	E_b U $4f_{7/2}$ (eV)	LW (eV)
UO_x–TiO_2	500, 700, 900	Ti $2p$ (458.6)	1.6	381.4 ↔ 381.6	2.1 ↔ 2.3
UO_x–MgO	500, 700, 900	Mg $2p$ (49.7)	1.4	381.4 ↔ 381.6	2.2 ↔ 2.5
UO_x–Al_2O_3	500, 700, 900	Al $2p$ (74.7)	1.7	381.7 ↔ 381.9	2.1 ↔ 2.3
UO_x–SiO_2	500, 700	Si $2p$ (103.6)	2.0	381.8 ↔ 382.0	2.0
	900	Si $2p$ (103.7)	2.0	380.6	2.8

not change with calcination temperature (the UO_x–TiO_2 sample shows a small decrease in the ratio as a function of increasing temperature).

XPS intensity ratios (I_U/I_c) are known to depend on many parameters, viz. concentration of the active phase, photoelectron cross sections, electron mean free paths (λ), support surface area, and the degree of dispersion of the supported phase. The porosity of the support is a further complication since XPS does not probe internal surfaces. It is therefore not possible to predict the dependence of (I_U/I_c) on the corresponding surface area, especially for high-surface-area carriers (*22*). No corrections for photoionization cross sections and mean escape depths of photoelectrons were made, as only relative comparison of the different samples was considered. When the supported phase is present as crystallites, the XPS intensity ratios I_U/I_c will decrease with increasing particle size of U_3O_8, since a lower fraction of the uranium atoms will contribute to the XPS signal. As shown in Fig. 6, the surface compositions illustrated by the XPS atomic ratios ($I_{U\,4f_{7/2}}/I_{M\,2p}$) depend strongly on calcination temperature. Generally speaking, it is expected that calcination temperature will affect the dispersion of the uranium oxide at the surface (probed by XPS) which, in turn, is influenced by crystallite size and by the possible formation of highly dispersed phases or of mixed compounds by interaction with the support. Usually, the dispersion decreases at high temperature (sintering). Segregation phenomena can also occur during calcination, decreasing the interfacial energy.

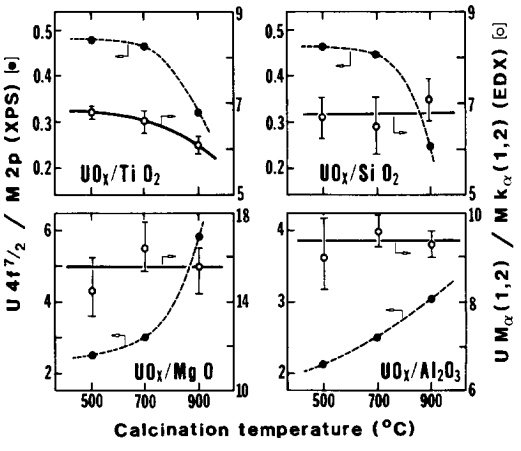

FIG. 6. Relative XPS intensity ratios ($I_{U\,4f_{7/2}}/I_{M\,2p}$) and corresponding EDX ratios ($I_{U\,M\alpha(1,2)}/I_{MK\alpha(1,2)}$) vs calcination temperature (M = Ti, Si, Mg, Al).

The relative intensity of U $4f_{7/2}$ XPS peaks decreases with temperature for UO_x deposited on SiO_2 and TiO_2. These results are consistent with the formation of larger aggregates of U_3O_8 (confirmed by TEM for UO_x–SiO_2), but they suggest also that the crystallites could be covered by a thin layer of support. Transportation of the support onto the UO_x species would result in their

TABLE 4

Melting Point and Estimated Tammann Temperature of Different Supports (Al_2O_3, TiO_2, SiO_2, MgO)

	Support				
	SiO_2	TiO_2 (rutile)	Al_2O_3	MgO	U oxides
Melting point (°C)	1723	1830–1850	2072	2852	Decompose above 1000°C
Estimated Tammann temperature (°C)	~765	~826	~946	~1352	

partial encapsulation and inhibit their detection by XPS. Such a phenomenon has been observed by Lund and Dumesic for SiO_2 (*20, 21*) and by Santos *et al.* for TiO_2 (*23*). It was also mentioned by Derouane (*24*) in the case of multimetallic catalysts. In the present case, this effect occurs at high temperature and it is reasonable to assume that migration is mainly directed by surface tension phenomena: the constituent with the lowest free energy tends to migrate to the surface to reduce the surface energy of the system. Mobility of a solid is expected to occur when it is at or above its Tammann temperature, which is approximately 0.52 T_m, where T_m is the melting point (in K) (*25*). Such a situation is encountered for TiO_2 and SiO_2 at 900°C (Table 4). Encapsulation could account for the strong interaction between UO_x species and SiO_2, suggested by the XPS chemical shift for the uranium signal in the UO_x–SiO_2 system calcined at 900°C (Fig. 6).

Opposite variations, namely an increase of the uranium XPS signal with increasing temperature, were observed for the MgO- and Al_2O_3-based catalysts (note that the Tammann temperatures for these carriers are well above 900°C, Table 4). Rejecting the possibility of forming smaller aggregates at high temperature, which is in contradiction with the more probable sintering, these observations are best explained by a migration of UO_x species to the surface in order to reduce the surface energy of these refractory supports. Catalytic data (*15*) support these interpretations.

CONCLUSIONS

We have shown that U_3O_8 is readily produced by thermal decomposition of uranyl nitrate. It can be stabilized on various supports at high temperatures.

We have particularly emphasized the importance of the calcination temperature on the structural and electronic properties of such phases. Interactions between the support and the U-containing precursor were observed. They influence the degree of dispersion of the supported species in the finished catalyst and hence its activity (*15*). In particular formation of a strong oxide–oxide interaction (SOOI) in the UO_x–SiO_2 system is confirmed by the chemical shift and the relative intensity variation of the uranium signal observed using XPS.

Sintering effects and segregation phenomena are suggested to predominate at high temperatures for uranium oxides. Our results suggest that encapsulation of uranium particles during calcination at 900°C takes place in the case of TiO_2 and SiO_2 supports. Segregation of UO_x species to the surface probably occurs for the more refractory carriers, Al_2O_3 and MgO. All these results are in agreement with the reduction of the surface energy of these systems. The new properties generated at high temperatures by the mobility in these solids will be

used to explain the drastic changes of their catalytic properties (*15*).

ACKNOWLEDGMENTS

The authors wish to acknowledge Solvay et Cie for the porosity measurements. One of us (H.C.) is grateful to IRSIA (Belgium) for a doctoral fellowship.

REFERENCES

1. Nozaki, F., and Inami, I., *Nippon Kagaku Kaishi* **11,** 2202 (1972).
2. Nozaki, F., and Inami, I., *Nippon Kagaku Kaishi* **10,** 1855 (1974).
3. Nozaki, F., and Ichikawa, F., *Nippon Kagaku Kaishi* **2,** 254 (1973).
4. Nozaki, F., and Ohki, K., *Bull. Chem. Soc. Japan* **45,** 3473 (1972).
5. Nozaki, F., Kobayashi, M., and Yoshida, S., *Nippon Kagaku Kaishi* **1,** 26 (1972).
6. Callahan, J. L., and Gertisser, B., U.S. Patent, 3,308,151 (1967).
7. Callahan, J. L., and Gertisser, B., U.S. Patent, 3,198,750 (1965).
8. Grasselli, R. K., and Suresh, D. D., *J. Catal.* **25,** 273 (1972).
9. Keulks, G. W., Yu, Z., and Krenzke, L. D., *J. Catal.* **84,** 38 (1983).
10. Baussart, H., Delobel, R., Le Bras, M., Le Maguer, D., and Leroy, J. M., *J. Chem. Soc., Faraday Trans. 1* **78,** 485 (1982).
11. Maroie, S., Collette, H., Gabelica, Z., Verbist, J. J., and B.Nagy, J., *Acta Chim. Acad. Sci. Hung.*, in press.
12. Steenhof de Jong, J. G., and Batist, P. A., *Recl. Trav. Chim. Pays-Bas* **90,** 749 (1971).
13. Steenhof de Jong, J. G., Guffens, C. H. E., and van der Baan, H. S., *J. Catal.* **26,** 401 (1972).
14. Nozaki, F., Matsukawa, F., and Mano, Y., *Bull. Chem. Soc. Japan* **48**(10), 2764 (1975).
15. Collette, H., to be published.
16. Lecloux, A., *Mem. Soc. R. Sci. Liège Collect. 4°* **1,** 169 (1971).
17. Verbist, J., Riga, J., Pireaux, J. J., and Caudano, R., *J. Electron Spectrosc. Relat. Phenom.* **5,** 193 (1974); Teterin, Y. A., Kulakov, V. M., Baev, A. S., Nevzorov, N. B., Melnikov, I. V., Streltsov, V. A., Mashirov, L. G., Suglobov, D. N., and Zelenkov, A. G., *Phys. Chem. Miner.* **7,** 151 (1981).
18. Lund, C. R. F., and Dumesic, J. A., *J. Phys. Chem.* **85,** 3175 (1981).
19. Lund, C. R. F., and Dumesic, J. A., *J. Phys. Chem.* **86,** 130 (1982).
20. Lund, C. R. F., and Dumesic, J. A., *J. Catal.* **72,** 21 (1981).
21. Lund, C. R. F., and Dumesic, J. A., *J. Catal.* **76,** 93 (1982).
22. Kerkhof, F. P. J. M., and Moulijn, J. A., *J. Phys. Chem.* **83,** 1612 (1979).
23. Santos, J., Phillips, J., and Dumesic, J. A., *J. Catal.* **81,** 147 (1983).
24. Derouane, E. G., *J. Molec. Catal.* **25,** 51 (1984).
25. Tammann, G., *Z. Angew. Chem.* **39,** 869 (1926).